Ultrafast Science
A SCIENCE PARTNER JOURNAL

Review Article

Theoretical Insights into Ultrafast Dynamics in Quantum Materials

Mengxue Guan [iD],[1,2] **Daqiang Chen** [iD],[1,2] **Shiqi Hu,**[1,2] **Hui Zhao,**[1,2] **Peiwei You** [iD],[1,2] **and Sheng Meng** [iD][1,2,3]

[1]*Beijing National Laboratory for Condensed Matter Physics and Institute of Physics, Chinese Academy of Sciences, Beijing 100190, China*
[2]*School of Physical Sciences, University of Chinese Academy of Sciences, Beijing 100190, China*
[3]*Songshan Lake Materials Laboratory, Dongguan, Guangdong 523808, China*

Correspondence should be addressed to Mengxue Guan; mxguan@iphy.ac.cn and Sheng Meng; smeng@iphy.ac.cn

The last few decades have witnessed the extraordinary advances in theoretical and experimental tools, which have enabled the manipulation and monitoring of ultrafast dynamics with high precisions. For modeling dynamical responses beyond the perturbative regime, computational methods based on time-dependent density functional theory (TDDFT) are the optimal choices. Here, we introduce TDAP (time-dependent ab initio propagation), a first-principle approach that is aimed at providing robust dynamic simulations of light-induced, highly nonlinear phenomena by real-time calculation of combined photonic, electronic, and ionic quantum mechanical effects within a TDDFT framework. We review the implementation of real-time TDDFT with numerical atomic orbital formalisms, which has enabled high-accuracy, large-scale simulations with moderate computational cost. The newly added features, i.e., the time-dependent electric field gauges and controllable ionic motion make the method especially suitable for investigating ultrafast electron-nuclear dynamics in complex periodic and semiperiodic systems. An overview of the capabilities of this first-principle method is provided by showcasing several representative applications including high-harmonic generation, tunable phase transitions, and new emergent states of matter. The method demonstrates a great potential in obtaining a predictive and comprehensive understanding of quantum dynamics and interactions in a wide range of materials at the atomic and attosecond space-time scale.

1. Introduction

Creating and controlling the macroscopic properties of quantum materials continue to improve our fundamental understanding of the underlying interactions among different degrees of freedom, which are of vital importance in designing new functionalities [1–3]. The rapid developments in the generation and synthesis of intense light pulses with a precisely controlled electric field provide a promising route to dynamically decouple and manipulate the microscopic interactions with an unprecedented time resolution (i.e., femtosecond or even attosecond) [4–11]. The nonlinear response of quantum materials to intense laser fields induce the emergence of various unexpected phenomena, including high harmonic generation (HHG) [12, 13], nonlinear photo-electron emission [14, 15], material melting, and phase transitions [16, 17]. These ultrafast processes are probed and understood by a new generation of experimental and theoretical tools and in turn provide insights into intrinsic properties of the system [18–20].

The mechanisms behind many of the most intriguing nonequilibrium phenomena go beyond the linear response theory. They are of great interest, but the detailed investigation especially from a theoretical aspect remains rather limited. To track the ultrafast dynamics in a nonperturbative regime, the real-time evolution of coupled electronic and ionic motion is required, which can be obtained by resorting to time-dependent density functional theory (TDDFT) approaches [21–23]. Therefore, real-time TDDFT represents a unique first-principle quantum method applicable for the

exploration of strong field physics and decoding vast information underneath the experimentally detected signals [24–26].

Under an external field, traditional Born–Oppenheimer (BO) approximation is not valid anymore to describe the strongly coupled electronic and nuclear motion, where the adiabatic electronic dynamics around the "frozen" nuclei is assumed. Understanding complex nonadiabatic dynamics is of great significance for the development of modern science and technology, which requires numerical solutions of time-dependent Schrödinger equation (TDSE) within a many-body theory framework. However, suffering from high computational costs, full quantum dynamics simulations (e.g., multiconfiguration time-dependent Hartree [27] and multiple spawning approaches [28]) are conventionally limited to rather small systems that contain only a few to tens of atoms. One of the practical strategies to reduce the computational costs is the mixed quantum–classical dynamics, where some degrees of freedom are treated classically and others obey quantum mechanics. These approaches include fewest switches surface-hopping algorithm [29], nonadiabatic Bohmian dynamics [30], quantum–classical Liouville dynamics [31], coupled-trajectories mixed quantum–classical method [32], and Ehrenfest dynamics [33, 34], which enable the possibility of simulating dynamics of large-scale realistic materials.

In this work, we review the implementation of first-principle rt-TDDFT algorithms with a numerical atomic orbital formalism, which is named as time-dependent ab initio propagation (TDAP) approach [35–37]. The time-domain quantum evolution of electronic states with the classical approximations of nuclear motions are treated concurrently in the scheme of Ehrenfest dynamics, which has enabled real-time tracking of coupled electron-nuclear dynamics in large-scale systems. The powerful predicting ability and broad application scopes of this approach are certified by introducing several quintessential works involving complex interactions among photons, electrons, and phonons under laser excitation conditions. For example, the generation of ultrashort laser pulses via HHG [38] and their uses for probing the essential electronic characteristics of solids, such as the carrier relaxation [39], band dispersion [40], and electron density [41]. Photoinduced ionic movements are also investigated; the resultant topological phase transitions and new collective modes are identified in Weyl semimetal WTe_2 [42] and charge density wave (CDW) materials $1T\text{-}TiSe_2$ [43] and $1T\text{-}TaS_2$ [44], respectively.

2. Theoretical Methodology

The Hamiltonian of a coupled electronic and nuclear system is defined as

$$\hat{H}_{\text{tot}}(r, R, t) = \hat{T}_{el} + \hat{T}_N(R) + V(r, R) + U_{\text{ext}}(r, R, t),$$
$$V(r, R) = \sum_{i<j} \frac{e^2}{|r_i - r_j|} - \sum_{i,\alpha} \frac{eZ_\alpha}{|r_i - R_\alpha|} + \sum_{\alpha,\beta} \frac{Z_\alpha Z_\beta}{|R_\alpha - R_\beta|},$$
$$(1)$$

where R and r are the collective coordinates of nuclear and electronic positions R_α, r_i, Z_α is the charge of the αth nucleus. $\hat{T}_{\text{el}}$, $\hat{T}_N$, and U_{ext} represent the electronic kinetic energy, nuclear kinetic energy, and external potential, respectively. Under the external field U_{ext}, the electronic Hamiltonian can be expressed as

$$\hat{H}_{\text{eff}}(r, R, t) = \hat{T}_{\text{el}} + V(r, R) + U_{\text{ext}}(r, R, t), \quad (2)$$

and a mean field of electronic states is obtained by

$$U(R, t) \equiv \int dr \psi^*(r, t) \hat{H}_{\text{eff}}(r, R, t) \psi(r, t), \quad (3)$$

where $\psi(r, t)$ represents electronic wavefunctions. With classical approximation of nuclear motion, the nuclear wavefunction $\chi(R, t) \approx \sum_\alpha \delta(R(t) - R_\alpha(t))$, and the time-evolution of $\psi(r, t)$ is parametrically dependent on the classical nuclei positions, which is written as

$$i\hbar \frac{\partial}{\partial t} \psi(r, t; R_t) = \hat{H}_{\text{eff}}(r, R, t) \psi(r, t; R_t). \quad (4)$$

An auxiliary system of noninteracting (Kohn-Sham) electrons is utilized in density functional theory to simplify the solution of electronic wavefunctions. Following this idea, Equation (4) is reduced to the time-dependent KS (TDKS) equation (Runge-Gross theorem [21]):

$$i\hbar \frac{\partial}{\partial t} \varphi(r, t) = \hat{H}_{\text{KS}}(r, R, t) \varphi(r, t), \quad (5)$$

where $\varphi(r, t)$ are the KS orbitals and $\hat{H}_{\text{KS}}(r, R, t) = \hat{T}_{\text{el}} + \sum V_I^{\text{KB}} + \sum V_I^{\text{local}}(r) + V^{\text{XC}}(r, t) + V^H(r, t) + U_{\text{ext}}(r, R, t)$. Here, V_I^{KB} and $V_I^{\text{local}}(r)$ are the Kleinman-Bylander and local parts of the pseudopotential of atom I, while $V^{\text{XC}}(r, t)$ and $V^H(r, t)$ are the exchange-correlation (XC) and Hartree potentials, respectively.

Several different technical approaches have been proposed to solve the TDKS equation. For example, in the well-known program packages such as SALMON [22] and OCTOPUS [23], real-space grids (RSGs) are used, whereas full potential linearized augmented planewaves (FP-LAPW) and grid-based projector augmented wave (GPAW) methods have been implemented in the ELK [45] and GPAW [46] codes, respectively. In the TDAP approach, the TDKS equations are solved by real-time propagation of wavefunctions in numerical atomic orbital (NAO) basis sets, which endow the method several advantages over available approaches, as discussed below.

(i) To describe a system with N_a atoms, $10^3 \times N_a$ to $10^4 \times N_a$ RSGs or PWs have to be invoked, while only $10 \times N_a$ NAOs are required. The adoption of overwhelmingly efficient NAO has enabled the high-accuracy simulation of complex materials ($N_a \approx 1000$) for a long time (on the order of picosecond). For examples, comparing to the real-grid

code OCTOPUS, the TDAP approach can acceler-ate the simulation efficiency by ~10 times for capped (10, 0) carbon nanotube with $N_a = 210$ and metallic clusters Ag_{55} with $N_a = 55$, assuming the same pseudopotentials, exchange correlation func-tionals, and laser waveforms have been used in the two approaches. [36]

(ii) The many-electron density propagates self-consistently at each nuclear and electronic steps, and forces are calculated based on mean-field the-ory. They can offer real-time trajectories of excited state and a direct microscopic picture on ultrafast dynamics of electrons and nuclei on the attosecond time scale.

(iii) Owing to the linear combination of NAOs, elec-tronic states localized near the atomic nucleus can be treated efficiently in the present approach. It is promising to realize simulations aiming at understanding the strong field driven inner shell excitation.

In NAO basis sets, the orbitals are not orthogonal. Adopting the periodic boundary conditions, at each k point, the Hamiltonian H_k and overlap matrix S_k are expressed as

$$S_{i\alpha,j\beta,k} = \sum_s e^{-ik \cdot R_s} \langle \xi_{i\alpha}(r + R_s + b_i) | \xi_{j\beta}(r + b_j) \rangle,$$
$$H_{i\alpha,j\beta,k} = \sum_s e^{-ik \cdot R_s} \langle \xi_{i\alpha}(r + R_s + b_i) | \hat{H}_{KS} | \xi_{j\beta}(r + b_j) \rangle. \quad (6)$$

Here, R_s ($s = 1, 2, 3, \cdots, N_c$) denotes the lattice vectors and $\xi_{i\alpha}$ is the NAO associated to atoms i that is located at b_i, where α denotes both the angular and orbital quantum numbers of the atomic state.

Two gauges, i.e., length gauge and velocity gauge, are optional for the TDKS equation to simulate the interaction between the diverse materials and laser field. Within the length gauge, time-dependent electric field $E(t)$ is intro-duced to the Hamiltonian via $U_{ext}(r, t)$,

$$U_{ext}(r, t) = -eE(t) \cdot r. \quad (7)$$

In this scenario, an auxiliary vacuum layer is required in the direction of electric field to avoid the energy divergence, which limits the approach only suitable for finite systems.

The adoption of velocity gauge is promising to overcome the limitations mentioned above. It can be applied to peri-odic system through a gauge transformation:

$$A = -c \int E dt, E = -\frac{1}{c} \frac{\partial A}{\partial t}, \quad (8)$$

where A is the vector potential. The electronic kinetic energy part in the TDKS equation can be expressed as

$$\hat{T}_{el} = \frac{1}{2m} \left(\hbar k - \frac{e}{c} A \right)^2 = \frac{1}{2m} \left(\hbar k + e \int E dt \right)^2. \quad (9)$$

The time evolution operator is approximated using first-order Crank-Nicholson scheme, and the time propagation of the TDKS equation is obtained as

$$|u_{nk}(r, t_2)\rangle \approx \exp\left[-iS_k^{-1}(t')H_k(t')\Delta t\right]|u_{nk}(r, t_1)\rangle, \quad (10)$$

$$\exp\left[-iS_k^{-1}(t')H_k(t')\Delta t\right] \approx \frac{1 - iS_k^{-1}H_k\Delta t/2}{1 + iS_k^{-1}H_k\Delta t/2}, \quad (11)$$

where $\Delta t = t_2 - t_1$ is the length of time step and $u_{nk}(r, t) = \varphi_{nk}(r, t)e^{-ik \cdot r}$ is the periodic part of Bloch function. With $u_{nk}(r, t_2)$ is solved, the density matrix $\rho_{i\alpha,j\beta}(t_2)$ is computed accordingly as

$$\rho_{i\alpha,j\beta}(t_2) = \sum_n \sum_k q_{n,k} c^*_{n,i\alpha,k}(t_2) c_{n,j\beta,k}(t_2), \quad (12)$$

where $q_{n,k}$ is electronic population of the band n at k and $c_{n,j\beta,k}(t_2)$ is the coefficient of $u_{nk}(r, t_2)$ in NAO basis,

$$u_{nk}(r, t_2) = \sum_{j\beta} c_{n,j\beta,k}(t_2) \xi_{j\beta}(r). \quad (13)$$

Within the classical limitation, in the mean field of elec-tronic states, the forces applied on the nuclei F_α are obtained from the following equation:

$$-F_\alpha(t) = \int dr \psi^*(r, t) \nabla_\alpha \hat{H}_{eff}(r, R, t) \psi(r, t). \quad (14)$$

$$\hat{H}_{eff} = \frac{1}{2m} \left(\hbar k - \frac{e}{c} A \right)^2 + \sum V_I^{KB} + \sum V_I^{local}(r) + V^{XC}(r, t) + V^H(r, t). \quad (15)$$

For a broad spectral range, e.g., visible and near-infrared lights, the effect on ions is intermediated by the electronic sub-system via electron-phonon couplings. However, when the laser frequency is low enough, i.e., terahertz, the phonon modes can be directly excited.

Equations (10) and (14) represent the coupled electron-nuclear dynamics. The time-dependent Newtonian motion of ions and the Kohn-Sham equations of electrons are solved simultaneously. Figures 1(a) and 1(b) show the flowchart of real-time excited state simulation at a given ionic step, and the schematic evolution of potential energy surface (PES) upon the photoexcitation.

In this review, we focus our attention on the nonlinear phenomena induced by the electric field component of lasers, and the TDKS equation in both the length and veloc-ity gauges formally neglect the effect of the external magnetic field. Indeed, by applying a chiral, e.g., left- or right-handed vector potential A in velocity gauge, the electrons of different orbitals can be selectively excited and the corresponding spin can be flipped via spin-orbital interactions, thus exhibiting magnetic moments in opposite directions. From the Dirac
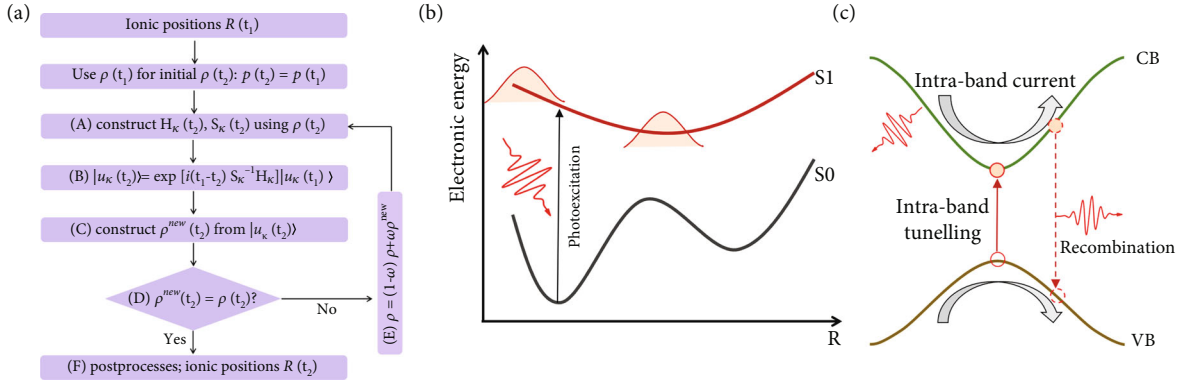
FIGURE 1: (a) Flowchart of rt-TDDFT approach for evolution of coupled electronic and ionic systems. Here, we assume that the two subsystems have the same evolution time step (~10 attosecond). (b) The scheme of quantum electronic and nuclear dynamic evolution. Upon the photoexcitation, electrons are excited from the ground-state potential energy surface (PES) (S0) and ions move on an excited PES (S1). (c) Real-space picture for solid-state HHG.

equation, we can obtain the KS Hamiltonian that contains the interaction between spin and the magnetic field

$$H_{KS}(t) = \left(-\frac{1}{2}\left(\hbar k - \frac{e}{c}A \right)^2 + V_H + V_{XC} - e\phi \right)I - \mu_B(B_{XC} + \nabla \times A) \cdot \sigma,$$

(16)

where I, μ_B, and σ denote the unitary matrix, the Bohr magneton, and the Pauli matrix, respectively. The second term $\mu_B(B_{XC} + \nabla \times A) \cdot \sigma$ indicates the magnetic field generated by the exchange correlation potential and the interaction between the external magnetic field $\nabla \times A$ and spin. Based on Equation (16), the module aimed at describing nonequilibrium spin dynamics is under development and will be implemented in the TDAP approach, which is intriguing but beyond the scope of this review.

3. Applications towards Real-Time Tracking of Ultrafast Dynamics in Quantum Materials

Upon excitation with an ultrafast laser pulse, a quantum material will return to its equilibrium after several relaxation stages, during which the energy is first transferred to the electrons and then to the lattice degrees of freedom [6, 47]. Within about one hundred femtoseconds, the photon-carrier and carrier-carrier interactions are dominant in determining nonlinear behaviors. The carrier excitation, scattering and recombination lead to the generation of high-energy photons (e.g., via HHG) and photoelectrons, which are of vital importance in the development of modern ultrafast control and detection techniques, such as transmission electron microscopes (TEM) [48, 49] and time-resolved angle-resolved photoemission spectroscopy (tr-ARPES) [50, 51]. For a longer timescale (several picoseconds), the energy is transformed to the lattice via carrier-phonon couplings; the spontaneous phonon emission induces intricate structural dynamics including phase transitions and emergence of new quantum states. The nonthermal control over quantum materials on the ultrafast timescale in a flexible and

reversible manner is attracting continuous attentions in designing new materials with desirable functionalities.

In this section, several quintessential examples are introduced in detail to show the capability of the TDAP approach in investigating ultrafast dynamics in quantum materials. We mainly focus on two topics: firstly, nonlinear effects related to HHG are displayed in prototypical systems, which are used to generate ultrashort laser pulses and to reconstruct the target electronic properties in both the ground and excited states. Secondly, the coupled electron-phonon interactions during the laser-driven structural distortion are explored in CDW and topological materials to gain the fundamental insights into the interplay among different degrees of freedom. The nonequilibrium "hidden states" and induced topological phase transitions are predicted. The results establish the feasibility of the present approach in understanding complex nonadiabatic dynamics of excited states in a wide range of quantum systems at ultrafast timescales.

3.1. Fundamentals of HHG. High-order harmonic generation (HHG) is a nonlinear optical process originating from the interaction between an intense laser field and atoms, molecules, or crystals. The photon energies of the emitted light equal to integer multiples of that for the driving laser. The HHG from solid materials was first discovered not until 2011 in ZnO [52]. In contrast to the semiclassical three-step model that is applicable for the description of HHG from gas-phase atoms [53], two distinct mechanisms, i.e., the interband and intraband transitions, are proposed to interpret the interaction between an intense, ultrafast pulse and periodic lattice structures [12, 54]. For the interband process, the generated electron-hole pair is accelerated by the laser field and then subsequently recombines coherently, emitting a harmonic photon. While in the intraband mechanism, the anharmonic electronic current resulting from the oscillation of the photoexcited electrons (holes) occupying conduction (valence) bands leads to harmonic emission (Figure 1(c)). Therefore, HHG is now used to probe essential properties of a solid, such as the band topology, the band dispersion,

and the arrangement of atoms in the crystal lattice [55, 56]. Meanwhile, HHG provides charge dynamics in quantum system from the frequency-domain view. Complete characterization of emitted high harmonic light, i.e., its polarization, spectrum, and phase information allow us to decode the real-time electron dynamics in crystal [57, 58].

In the present approach, the time-dependent current density can be obtained as

$$J(t) = \frac{1}{2m} \int_\Omega dr \sum_i \{\psi_i^*(r,t)\pi\psi_i(r,t) + c.c\}, \quad (17)$$

and the generalized momentum

$$\pi = \frac{m}{i\hbar}\left[r, \hat{H}_{KS}\right] = -i\hbar\nabla + \frac{e}{c}A(t) + \frac{im}{\hbar}[V_I, r]. \quad (18)$$

The electron-ion interaction $V_I = V_I^{KB} + V_I^{local}$, where V_I^{local} and V_I^{KB} are the local and nonlocal pseudopotentials, respectively. The use of V_I^{KB} has enabled the transform of V_I between the velocity (V_{Iv}) and length gauges (V_{Il}) by

$$V_{Iv}\psi_i(\boldsymbol{r},t) = \int dr' \exp\left[-\frac{ie}{\hbar c}A(t)\bullet r\right]V_{Il}\left(r,r'\right)$$
$$\times \exp\left[\frac{ie}{\hbar c}A(t)\bullet r'\right]\psi_i(\boldsymbol{r},t). \quad (19)$$

The second term of π, i.e., $(e/c)A(t)$ leads to a diamagnetic current

$$J_d = \frac{e}{2mc}A(t)\int_\Omega dr \sum_i \{\psi_i^*(r,t)\psi_i(r,t) + c.c\},$$
$$n\left(\overrightarrow{r},t\right) = \sum_i \psi_i^*(r,t)\psi_i(r,t), \quad (20)$$
$$N_e = \int_\Omega dr\, n(r,t).$$

Here, $n(r,t)$ is the many-body electronic density and N_e is the number of electrons in the system, which is a constant. Based on that, the diamagnetic term of current reduces to $J_d(t) = eN_e/mcA(t)$, and the Fourier transform of $J_d(t)$ only contributes to the first order of HHG spectra. Since we only focus on the high-order response of the quantum material to the laser fields, in our code, the momentum is simplified as

$$\pi = -i\hbar\nabla + (im/\hbar)[V_I, r]. \quad (21)$$

The HHG spectrum is obtained through a Fourier transformation of $J(t)$,

$$\mathrm{HHG}(\omega) = \omega^2 \left|\int_0^T J(t)\exp(-i\omega t)dt\right|^2. \quad (22)$$

3.1.1. Ultrafast Optical Modulation of Harmonic Generation in Graphene. For nanooptoelectronic and nanophotonic

devices, the modulation of their optical properties is of vital importance due to the potential applications in optical interconnects, switching, and communication. All-optical strategies can reach an ultrafast modulation speed that is urgently needed in high-speed optical information processing. Here, we show that the third harmonic generation (THG) of a graphene monolayer can be dynamically modulated by the nonlinear dynamics of photoexcited carriers with a relative modulation depth of above 90% [39].

The unique gapless and linear two-dimensional (2D) band structure of graphene endows the strong light-matter interaction in both linear and nonlinear regimes. Due to the centrosymmetric crystal structure, only odd-order nonlinear optical response is allowed. We performed first-principle dynamics simulations that are analogous to the experimental pump-probe spectroscopic measurements (Figure 2(a)). The waveform of laser pulse is described to be a superimposition between the Gaussian-shaped pump and probe lights,

$$E(t) = E_1 \cos(\omega_1 t)\exp\left[-\frac{(t-t_0)^2}{2\sigma^2}\right]$$
$$+ E_2 \cos(\omega_2 t)\exp\left[-\frac{(t-(t_0-\Delta t))^2}{2\sigma^2}\right]. \quad (23)$$

Here, the two lasers have the same pulse width of $2\sigma = 8$ fs, and the ratio of laser fluence is $E_1^2/E_2^2 = 5.86$. The $\hbar\omega_1 = 3.1$ eV ($\hbar\omega_2 = 0.92$ eV) is the photon energy of the pump (probe) pulse, $t_0 = 15$ fs denotes the center of pump pulse and Δt is time delay between the two pulses. Here, THG signal of the probe pulse is detected.

The dependence of relative THG intensity on the delay time (Δt) is shown in Figures 2(c) and 2(d). At $\Delta t < 0$, the probe pulse gives a THG spectrum same as that from the pristine graphene, due to the fact that the pump pulse is not involved. When $\Delta t > 0$, the THG transition of the probe pulse is blocked by the preexcited carriers, leading to the decrease of THG intensity. Therefore, the suppressed coherent process in graphene is attributed to the nonlinear dynamics of the photoexcited carriers. The results represent an efficient route to utilize the ultrafast optical pump to engineer the harmonic generation of 2D materials.

3.1.2. Picometre-Scale Imaging of Valence Electrons in Solids. HHG in solids are primarily explained as the results of the nonlinear driving of carriers between and within electronic bands. The valence electrons will experience nonlinear scattering from the crystal potential, and thus, it is expected that the emitted harmonics contain the necessary information that enables real-space, picometre-scale mapping of the valence electron structure. Taking MgF_2 as an example, we show the strategy of using HHG spectrum to reconstruct the valence potential [41].

The atomic structure of MgF_2 is shown in Figure 3(a), which has a tetragonal geometry and a square lattice along the c-axis. The effective potential experienced by a valence electron can be suppressed with an external field, and
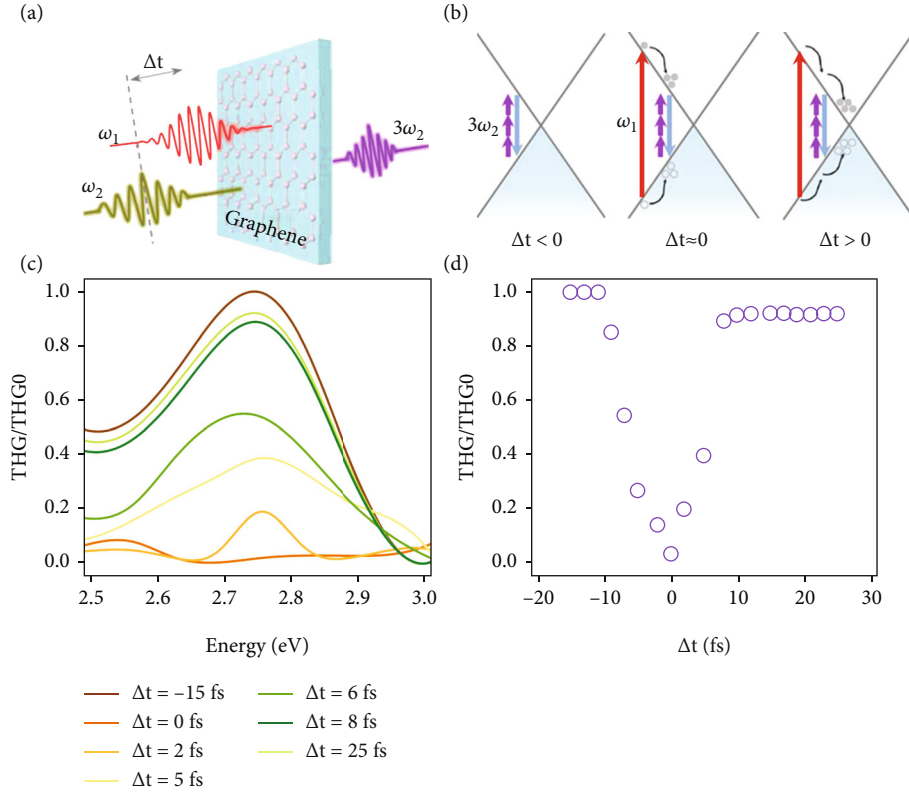
FIGURE 2: Optical modulation of THG from a graphene monolayer. (a) TDAP simulations that can be directly compared with the pump−probe spectroscopic measurement. (b) Schematic illustration of the ultrafast temporal dynamics of photoexcited carriers in graphene. (c) THG spectrum at a set of delay time between the 3.1 eV pump and the 0.92 eV probe. (d) Time evolution of the relative THG intensity.

quasi-free electron motion is expected. For a wide range of optical field strengths, the photocarriers velocity in the bulk MgF_2 ($v_c(t)$) is calculated and compared to that of the free electrons driven by the identical waveforms ($v_{free}(t)$) (Figure 3(b)). The velocity of the crystal electrons rapidly increases with the stronger field strength F_0, at the critical field $F_0 \approx 0.95$ V/Å, it reaches that of the free electrons, i.e., $v_c(t)/v_{free}(t) \approx 1$. When $F_0 > 0.95$ V/Å, the drop of $v_c(t)/v_{free}(t)$ is attributed to the Bragg reflection.

When the crystal potential is considerably suppressed, the dynamics of the electronic wavefunction and resultant high harmonic emission can be treated within the framework of scattering [59, 60]. The periodic potential and the intensity of the harmonics ($N\hbar\omega_L$) are linked via

$$I_N(F_0, \omega_L, e_l) \propto \left| N_e \sum_{k_l} \tilde{V}_{k_l} k_l J_N\left(k_l \frac{F_0}{\omega_L^2}\right) \right|^2. \quad (24)$$

Here, e_l is the laser polarization vector; $\tilde{V}_{k_l}$ and k_l are, respectively, the projections of the Fourier components of the potential and the reciprocal space vectors on to the e_l; and J_N is the Bessel function of the first kind and order N. Equation (24) implies that the Fourier components $\tilde{V}_{k_l}$ of a one-dimensional slice of the crystal potential can be retrieved by measuring a set of N harmonics with varied laser strengths F_0.

Representative harmonic spectra when the laser is polarized along the [110] crystal axes are shown in Figure 3(c). We record the harmonic intensities as a function of the optical field strength F_0, and the amplitudes and phases of $\tilde{V}_{k_l}$ are retrieved using Equation (24). The inverse Fourier transform of $\tilde{V}_{k_l}$ yields the reconstructed real-space potential shown in the inset of Figure 3(d), where the three consecutive valleys correspond to the potential of F⁻, Mg⁺², and F⁻ ions, fitting well with that calculated by the ground-state static DFT simulations. Similar reconstruction strategies can be extended to more crystal directions, e.g., [100] direction shown in Figure 3(e), to enable the direct measurement of the valence electron structure in solids with a picometre accuracy by using HHG.

3.1.3. Cooperation of Interband and Intraband Excitations in Strained MoS_2. The complicated interplay between interband and intraband transitions can be controlled in solid-state materials and utilized to improve the HHG performance. However, the coupling mechanism and relative contribution of the two processes are highly debated and may vary in different spectral ranges and materials [61–63]. Due to the fact that HHG is highly sensitive to the atomic and electronic structures, tailoring crystal structure via strain provides an effective tool helping clarify the microscopic mechanisms, especially for the 2D materials with an atomic thickness.
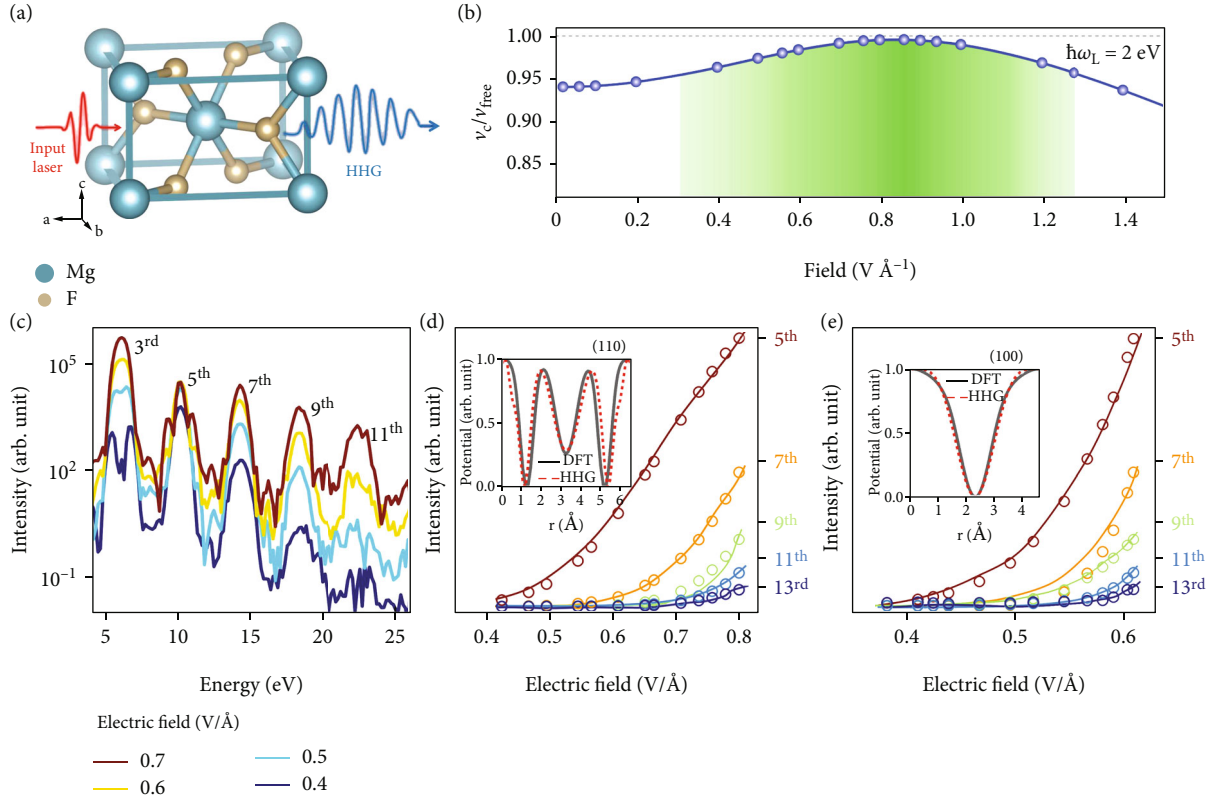
FIGURE 3: The reconstructed valence electron potential of MgF$_2$ via HHG spectra. (a) Schematics showing the high order harmonic generation in solid MgF$_2$. (b) Ratio of the maximum of crystal ($v_c(t)$) and free ($v_{free}(t)$) electron velocities along [100] direction of MgF$_2$ crystal as a function of field strength of the driving pulse with a carrier photon energy of 2 eV. (c) The HHG spectrum with electric field polarization along [110] direction. The HHG intensity as a function of electric field strength along [110] (d) and [100] (e) directions. The cycle symbols are the data points and the solid lines are the fitting lines. The insets in (d) and (e) shows the valence electron potential distribution along [110] and [100] directions. The solid black and dashed red lines label the potential obtained by the DFT calculation and HHG spectrum reconstruction, respectively.

Figure 4(a) shows the calculated HHG spectrum of monolayer (1 L) MoS$_2$, which is in good agreement with the experimental measurement [40]. The relative change in HHG intensity is linearly dependent on the strain amplitude, whereas the rates vary with the harmonic orders (Figure 4(b)). The fitting slopes of odd harmonics are generally smaller than the even ones, indicating that the two kinds of harmonics have different origins.

We first assume that the interband tunneling and carrier scattering are negligible, based on a semiclassical analysis related to the acceleration theorem [8],

$$v_{n,k}(t) = \frac{\partial \varepsilon_n(k,t)}{\hbar \partial k} - \frac{e}{\hbar} E \times \Omega_n(k,t). \quad (25)$$

We expect that the even- and odd-order harmonics exhibit significant dependence on materials' Berry curvature and band dispersion, respectively [8]. Compressive strain ($\varepsilon < 0$) will flatten both of them, leading to the increased intraband transition probabilities and harmonic yields.

For the interband process, the time- and momentum-resolved dynamics of excited electrons are investigated.

The number of photoexcited electrons (Δn) increases with lattice contraction (Figure 4(c)), indicating more carriers have been promoted to a broader (intraband) momentum space and higher energy levels (interband). To verify the above interpretation, momentum-resolved electron occupation is shown in Figure 4(d). It is clear that most of electrons are excited to the K and K' valleys of the Brillouin zone (BZ) of 1 L-MoS$_2$. Under compressive strain, the number of excited electrons at each momentum increase and they distribute at a lager fraction of the BZ simultaneously, which is direct evidence that intraband and interband dynamics enhance the harmonics yield cooperatively. When the tensile strain is applied, the results are reversed.

According to the acceleration theorem, in the intraband mechanism, an anomalous in-plane current that is perpendicular to the pump laser polarization is introduced by Berry curvature ($J \propto \dot{k} \times \Omega \propto E \times \Omega$). Nevertheless, the model fails to explain the emergence of *parallel* components, indicating contributions from interband dynamics are also present. Therefore, the relative contribution of interband and intraband processes to the harmonic generation can be identified via comparing the parallel and
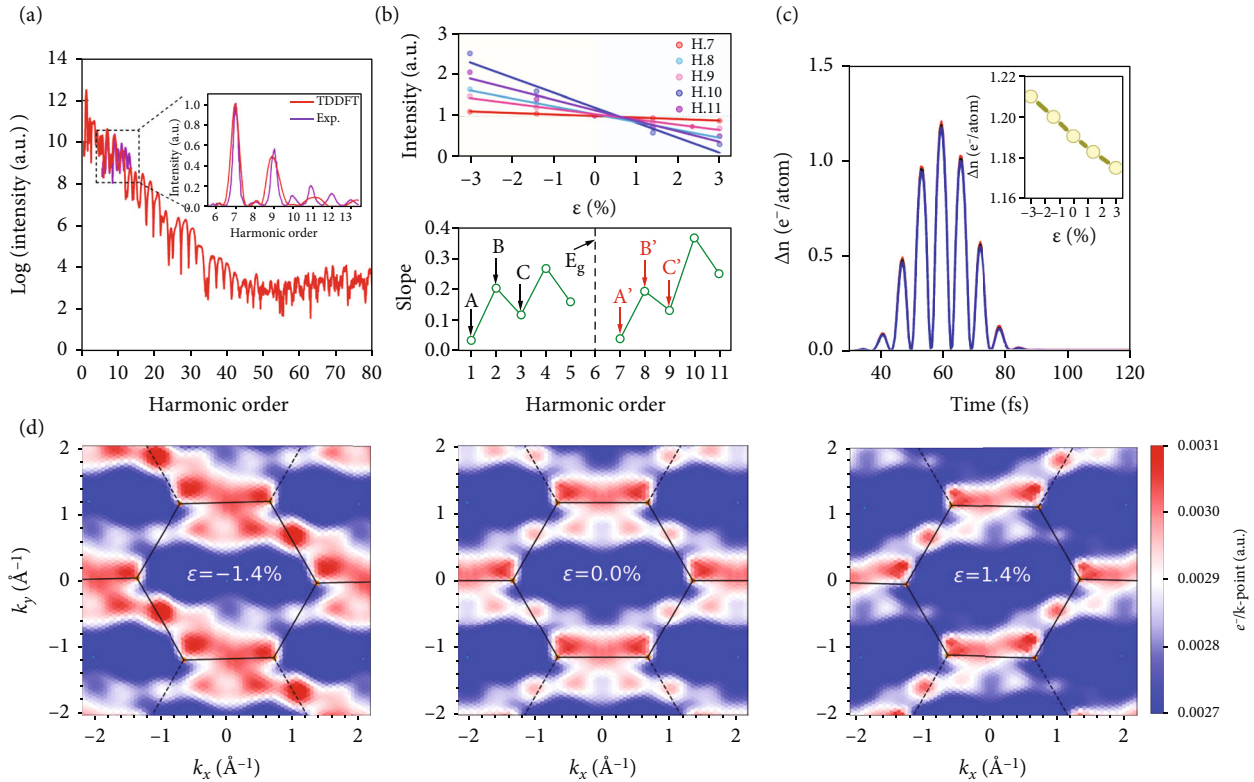
FIGURE 4: Electronic excitation mechanisms in strained 1 L-MoS$_2$. (a) HHG spectrum of primitive 1 L-MoS$_2$ from TDDFT calculation (red) and its comparison with the experimental measurement (purple). (b) Dependence of HHG intensity on the applied strain, and the absolute values of slope corresponding to representative harmonics. (c) Number of electrons excited to the conduction bands during the laser illumination. The inset shows the maximum value of excited electrons ($t = 60$ fs) as a function of strain. (d) Distribution of the photoexcited electrons in Brillouin zone at $t = 60$ fs under three strain conditions.
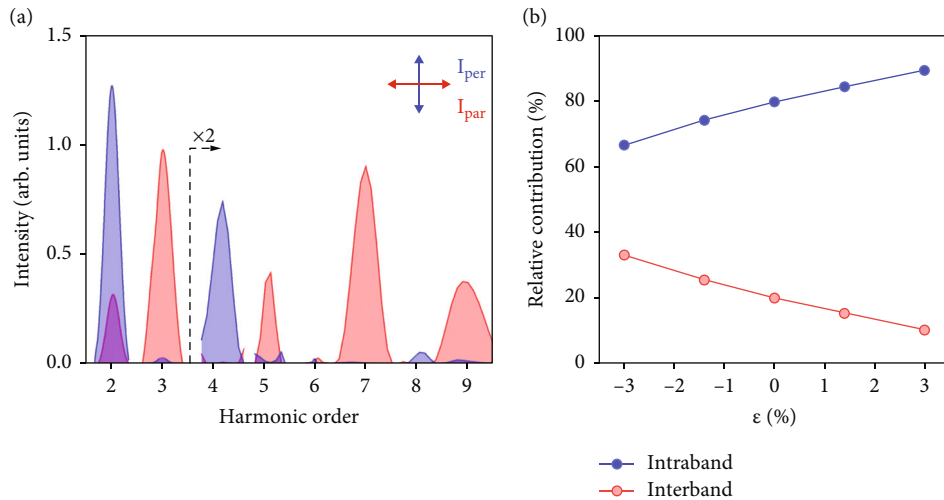

FIGURE 5: The relative contribution of intraband and interband excitation to HHG in a strained MoS$_2$. (a) Computed harmonic components that are parallel (red) and perpendicular (blue) to the linearly polarized excitation. (b) Evolution of intraband and interband contributions to the second-order harmonic generation as a function of the applied strain.

perpendicular components of even harmonics (Figure 5(a)). We find that the intraband transitions play a dominant role in harmonic radiation ($I_{intra}/I_{total} > 65\%$), while the compressive strain will enhance the proportion of interband contributions (Figure 5(b))

3.1.4. *The Generation of Ultrashort Laser Pulses in Solids.* Creating brighter and shorter isolated attosecond pulse (IAP) via HHG is one of the important goals in the ultrafast science community [64, 65]. IAP can be used to reveal microscopic details of the involved ultrafast processes, such
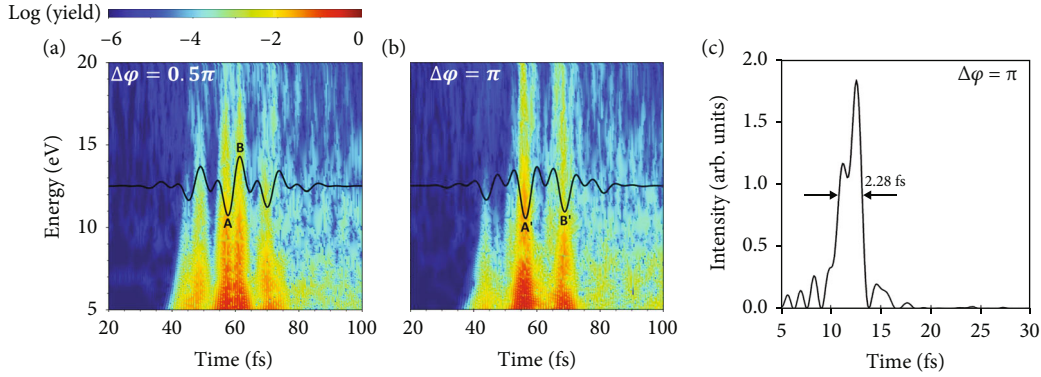
FIGURE 6: The dynamics of two-color laser driven harmonic emission. (a, b) Time-frequency analysis of the harmonic radiation when (a) $\Delta\varphi = 0.5\pi$ and (b) $\Delta\varphi = \pi$. The corresponding electric field waveforms are shown as the black lines. (c) The temporal profiles of the generated ultrashort pulse which is obtained by doing inverse Fourier transformation of the high energy part of (b).

as electron dynamics, bond creation, or breaking with an attosecond resolution. Controlling the driving pulse via tuning the second-pulse parameters of the two-color laser component has been widely adopted to tailor the harmonic emission of different systems from gases to liquids and solids [66, 67]. Here, we show that the optimized phase is critical for the modulation of HHG spectrum morphology and the generation of ultrashort isolated pulse in a solid material [38].

In our simulations, two monochromatic components linearly polarized along the zigzag direction of $1\,L$-MoS_2 are superimposed to synthesize the laser pulses, which are expressed as

$$E(t) = E_0 \exp\left[-\frac{(t-t_0)^2}{2\sigma^2}\right][\cos(\omega t) + \cos(2\omega t + \Delta\varphi)],$$

(26)

where the pulse width is 12 fs and the photon energy of the fundamental field is $\hbar\omega = 0.32$ eV. At time $t_0 = 60$ fs, the strength of the fundamental laser field reaches its maximum value of $E_0 = 0.056$ V/Å, and the relative phase between the two pulses is labeled as $\Delta\varphi$.

The dynamics of harmonic generation when $\Delta\varphi = 0.5\pi$ and $\Delta\varphi = \pi$ are shown in Figures 6(a) and 6(b), respectively. It is clear that suboptical-cycle waveform control is achieved by the participation of frequency-doubled pulse, leading to the modulation of spectrum morphology. When $\Delta\varphi = 0.5\pi$, fairly discrete harmonic peaks are produced by the interference between two extreme ultraviolet (EUV) bursts with comparable intensities (Figure 6(a)). However, when $\Delta\varphi = \pi$, the intensity of central peak ($A^{'}$) is much stronger than the remaining peaks (e.g., $B^{'}$), and a more continuous spectrum is produced by the single dominant EUV burst (Figure 6(b)).

A HHG spectrum with a broad spectral width and a flat profile is necessary to generate IAP. For the HHG spectrum when $\Delta\varphi = \pi$, a nearly-isolated ultrashort EUV pulse with a width of 2.28 fs is produced by doing an
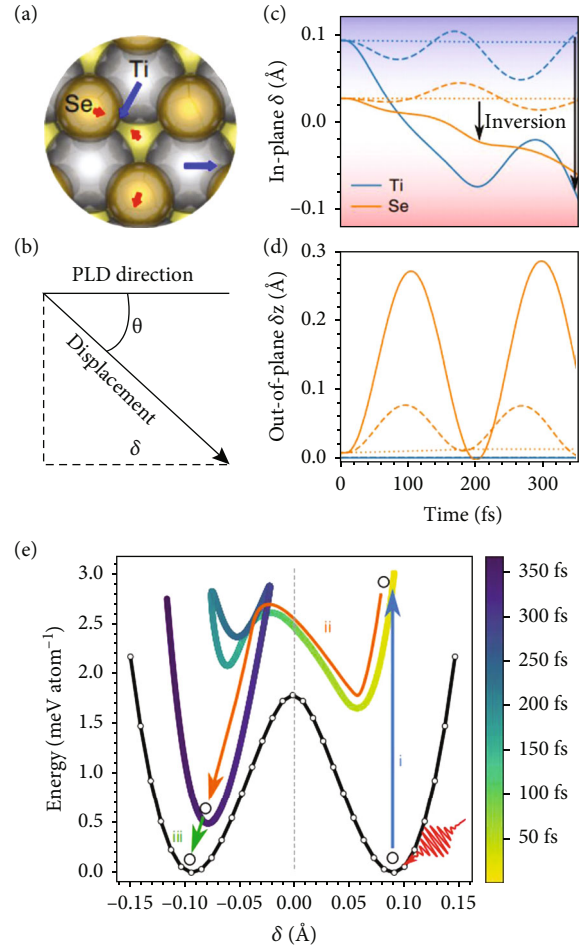

FIGURE 7: Photoexcited lattice dynamics in $TiSe_2$. (a) The nontrivial symmetrically inequivalent Ti and Se atoms with PLD. (b) Schematic diagram of in-plane displacement δ. (c, d) The in-plane and out-of-plane displacement δ, δ_z, respectively. (e) The curve marked by hollow circles and the other curve indicate the ground state potential energy surface (PES) and the nonequilibrium time-dependent PES, respectively.
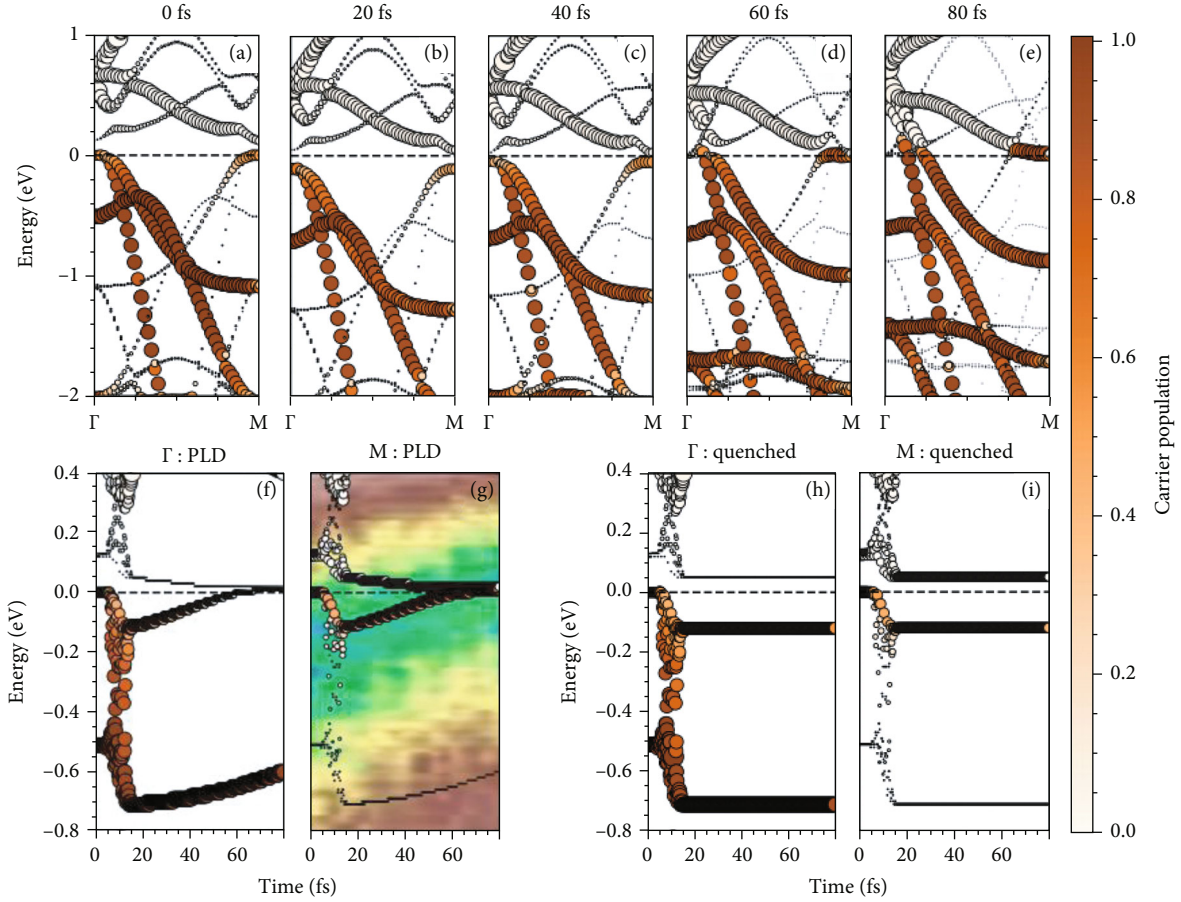
FIGURE 8: Time-dependent electronic band structure (TD-EBS) of $TiSe_2$ upon photoexcitation. (a–e) Snapshots of TD-EBS with the PLD dynamics. (f–i) Time-evolution of EBS at the Γ and M points with lattice distortion (f, g) and the quenched case (h, i). The color bar denotes the carrier population. The squares in (g) mark the experimental tr-ARPES data.

inverse Fourier transformation of the high-energy part (16~20 eV) (Figure 6(c)), which is much shorter than that of the incident laser. The results suggest that 2D materials are the potential candidates to generate tunable IAP with a clean temporal profile. The coherent EUV radiations generated from solids are expected to advance laser electronics and photonics to a multipetahertz frequency realm and can be applied to a broad range of scientific fields, such as tracing and control of electron dynamics in an attosecond timescale.

3.2. Laser-Driven Phase Transition in CDW and Topological Materials.
In the above discussions, the generated high harmonics are directly determined by the intrinsic electronic and lattice structures of target materials and can serve as an efficient tool to probe the essential properties, during which the phonon dynamics is negligible due to the ultrashort interaction duration (<100 fs). Ultrafast optical manipulation of crystal and electronic phase transition is another hot topic with intense discussion recently. Theoretical insights into explicit electron-phonon coupling mechanisms and nonequilibrium phase transition pathways upon photoexcitation, critical for modulating material and device performances, are of great interest but remain elusive. In the following sections, we introduce

the microscopic dynamic picture of phase transitions in CDW and topological materials, where a variety of quantum interactions and degrees of freedom coexist and are strongly coupled.

3.2.1. Self-Amplified Exciton-Phonon Dynamics in $TiSe_2$.
The CDW phase is the ground state of matter with a periodic modulation of charge density associated with a periodic lattice distortion (PLD) of the crystal [68]. The driving force for the formation of CDW in the archetypal CDW material $TiSe_2$ has been an eye-drawing question over decades. The relative contribution of PLD will identify the explicit mechanism, i.e., either electron-phonon couping (EPC) [69] or excitonic pairing [70], where in the former case, PLD is essential. In order to clarify the ultrafast CDW dynamics in $TiSe_2$, TDDFT molecular dynamics (TDDFT-MD) simulations are carried out [43].

A Guassian-envelope laser pulse is applied to 1T-$TiSe_2$ along the out-of-plane direction of its CDW ground state. The laser is centered at $t = 10$ fs and its wavelength, width, and fluence are 800 nm, 12 fs, and 2.1 mJ/cm^2, respectively. After the end of laser pulse (20 fs), the carrier density reaches it maximum value and is approximately proportional to the laser fluence. In the CDW $2 \times 2 \times 2$ phase, only one Se atom

and one Ti atom are symmetry-inequivalent in the single layer (Figure 7(a)). The time-dependent displacement $(d_i(t)(i = \text{Ti, Se}))$ along the PLD direction $(d_i(t_0))$ is defined as $\delta_i(t) = d_i(t) \cdot d_i(t_0)/|d_i(t_0)|$ (Figure 7(b)). During the simulations, the total energy $E_{\text{tot}}(t) = E_{kin}(t) + E_{kout}(t) + E_p(t)$ is conversed, where $E_{kin}(t)$, $E_{kout}(t)$, and $E_p(t)$ are the in-plane, out-of-plane kinetic energy, and potential energy, respectively. Therefore, $\Delta E_p(t) = -E_{kin}(t) - E_{kout}(t)$ represents the dynamical PES with in-plane PLD motion and trivial out-of-plane motion introduced by A_{1g} mode.

The dynamical PES evaluated from the simulations is shown in Figure 7. In the first 20 fs, the potential energy is raised as a result of carrier excitation from the bonding state to the antibonding state. During 20-300 fs, $\Delta E_p(t)$ decreases due to the in-plane movement antiparallel to the original direction of PLD (Figure 7(c)), while the oscillation can be attributed to the A_{1g} mode motion (Figure 7(d)). After 300 fs, the PLD motion is fully inversed and the dynamical potential energy falls into another local minimum, indicating a new quasi-equilibrium state that has an equivalent symmetry from the initial CDW state (Figure 7(e)).

The coupled lattice distortion and electronic dynamics are facilitated with each other and both serve as the driving force for the PLD inversion. Through analyzing the time-dependent electronic band structure (TD-EBS), we find that electronic structure closely relies on the ionic movements, which is in good agreement with experimental results [71] (Figure 8). For example, the band gap is closed due to laser-induced upward motions of valence bands, the formed electron-hole pockets boost the relaxation of photocarriers, and thus, the total energy of the system is decreased. Therefore, the self-amplification picture can be summarized as follows: the PLD is decreased → the band gap is vanished → the carrier energy is decreased → the further decrease in PLD.

Based on above analysis, an entangled electron-phonon mechanism is proposed for the presence of charge ordering in TiSe$_2$ that both EPC and exciton pairing contribute to the PLD/CDW formation but within different timescales: exciton pairing will trigger the formation of CDW within 20 fs, and subsequently, EPC can facilitate the dynamics via a self-amplification process. The reasonable agreements between our results and experimental data also confirm the reliability of our approach in treating EPC in the Ehrenfest scheme.

3.2.2. Creating a New Nonequilibrium State in TaS$_2$.
As discussed in the above example, the PES can be significantly modified by strong laser fields and ultrafast carrier-carrier scattering, which might lead to the emergence of new photoinduced phase via cooperative atomic motion. The phase dynamics of another typical CDW material 1T-TaS$_2$ have been widely studied in experiments recently, whereas the microscopic mechanisms concerning how the atomic and electronic motion are coupled remains elusive [72, 73]. Based on our first-principle nonadiabatic TDDFT-MD simulations, we find that upon strong photoexcitation, a novel collective oscillation mode between the CDW state and a new metallic state emerge, which cannot be reached by thermal phase transitions [44].
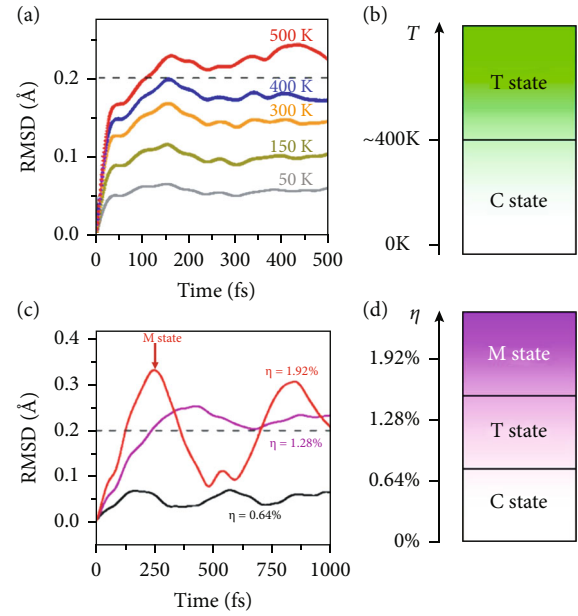

FIGURE 9: The evolution of atomic structure of 1T-TaS$_2$ under various thermal and photoexcitation conditions. (a) RMSD of 1T-TaS$_2$ under different ionic temperatures (T), the results are obtained from Born-Oppenheimer molecular dynamics (BOMD) simulations. (b) Phase diagram under thermal activation. (c) Time evolution of RMSD under different laser intensities calculated from the nonadiabatic MD simulations. (d) Phase diagram under laser excitations.

The bulk 1T-TaS$_2$ in its CDW state is simulated with a supercell of 78 atoms with $\sqrt{13} \times \sqrt{13} \times 2$ periodical boundary conditions and only the phonon modes at the Γ point are considered to play the dominant role in determining the nonequilibrium dynamics. We adopt standard Verlet algorithm for molecular dynamics, and the temperature is controlled by means of a Nosé thermostat to investigate the thermal-induced phase transition. For laser excitation condition, an initial temperature of 10 K is set, and during the structural evolutions, no extra temperature control strategy is adopted, namely, using a microcanonical ensemble.

The dynamics of CDW phase in 1T-TaS$_2$ under different thermal and laser conditions was investigated. To quantify the lattice structure changes, root-mean-square displacement of all atoms, RMSD $= \sqrt{u^2}$ is recorded, where $u(t)$ is the atomic displacement relative to the ground-state CDW state. As the ionic temperatures rises, the equilibrium value of RMSD increases and the CDW state reaches its melting threshold at $T_c \approx 400$ K, when the critical value of RMSD is $R_c = 0.2$ Å (Figure 9(a)). Above T_c, the characteristic "star of David" (SD) pattern of CDW phase starts to disappear, and the lattice restore its high-temperature undistorted 1T phase (referred to as the T state) (Figure 9(b)).

We find that for 1T-TaS$_2$, photoinduced ionic dynamics is distinct from the thermal activation, as shown in Figure 9(c). We use a Gaussian-envelope function to describe the applied laser pulses with the photon energy and width are 1.6 eV and 11 fs, respectively. The carrier
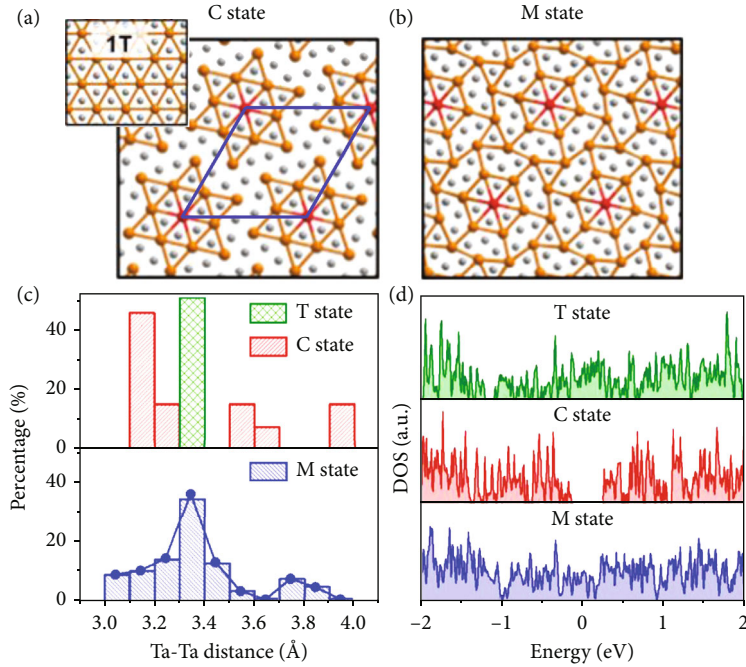
FIGURE 10: Atomic and electronic properties of the three states in 1T-TaS$_2$. Atomic structure of 1T-TaS$_2$ in CDW state with a $\sqrt{13} \times \sqrt{13}$ superlattice (blue rhombus). Inset shows the undistorted 1T phase of bulk TaS$_2$. (b) Atomic structure of the laser induced M state. (c) Radial distribution of Ta-Ta distances in different states. The T phase is presented in green with the nearest Ta-Ta distances of 3.36 Å. (d) In-plane density of states (DOS) for the three states.

density and the atomic displacement can be tuned by modulating laser fluences. At low laser intensity with a small percentage (η) of valence electrons excited to conduction bands ($\eta = 0.64\%$, 0.25 mJ/cm^2), the RMSD is slightly modulated with a period of ~400 fs, attributing to the excitation of the amplitude mode of CDW state (~2.3 THz). When η is increased to 1.28% (0.50 mJ/cm^2), the SD pattern melts at ~250 fs after photoexcitation. At 440 fs, the corresponding RMSD reaches a maximum value of 0.25 Å and then keeps stabilized at the value larger than R_c, indicating the phase destruction. When the laser intensity is further increased to excite plenty of carriers of $\eta = 1.92\%$ (0.75 mJ/cm^2), the electron-nuclear dynamics show distinctive behaviors where the SD pattern collapses rapidly and a new transient state appears at ~250 fs (referred to as the M state). Meanwhile, the RMSD reaches its maximum value (0.32 Å) and shows an oscillation with a period of 480 fs. The SD pattern is recovered when the RMSD swings down to 0.1 Å.

The structural and electronic properties of the M state are distinct from the CDW state and T state, as shown in Figure 10. The undistorted T state has the uniform Ta-Ta distances of 3.36 Å, whereas in M state, a new Ta-Ta distance around 3.75 Å emerge between the atoms in the regular central hexagons and those in the outer rings, indicating the photoinduced M state is far from the T phase. In addition to the difference in atomic structures, electron densities of states of two phases are also different. Despite both T and M states are metallic, T state has a sharper dispersion at Fermi level compared to M state. As a result, the features in optical absorption for T and M states are also different.

The ionic temperature keeps below T_c during the photo-induced phase transformation (<300 K), therefore, the newly emerged M state cannot be reached thermally and is closely related to the intrinsic electron-nuclear coupling. The results also clarify that the breakdown of hot-electron model due to its lack of electron-electron scattering, and thus provide a deep insight into understanding a wide range of laser induced phenomena in CDW materials.

3.2.3. Controllable Topological Phase Transition by Orbital-Selective Photoexcitation. Ultrafast manipulating of topological invariants is very important in understanding the fundamental properties of quantum materials and might be applied to design new optoelectronic devices with excellent performance. As a potential type-II Weyl semimetal, T$_d$-WTe$_2$ has recently garnered significant scientific interests in research frontiers [51, 74, 75]. In our recent work, linearly polarized laser pulses with a varied polarization vector and photon energy are applied to T$_d$-WTe$_2$ to study its optoelectronic responses [42].

The atomic structure of T$_d$-WTe$_2$ is shown in Figure 11(a), the two layers without inversion symmetry are bonded via van der Waals (vdW) interactions in the orthorhombic unit cell. We find that when a near-infrared laser pulse (ca. 0.6 eV) is applied, the interlayer shear displacement shows a polarization-anisotropic response, as shown in Figures 11(b) and 11(c). When the laser is polarized along the crystallographic a-axis (LP-a), the top (bottom) layer moves towards the negative (positive) direction of the b-axis, leading to the restoring of inversion symmetry in the 1T′ phase. However, under LP-b excitation, the relative
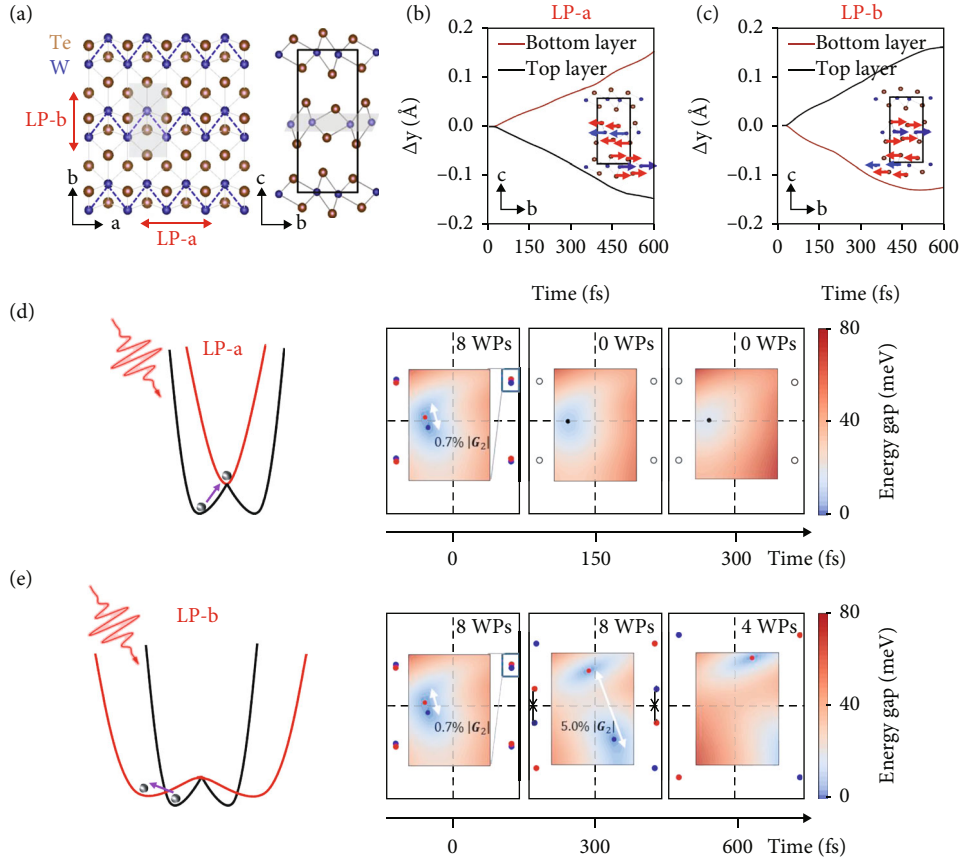
FIGURE 11: Polarization-anisotropic response of interlayer shear displacements and the induced topological phase transitions. (a) Top and side views of lattice structure of T_d-WTe$_2$. (b, c) Interlayer shear displacements when the laser polarization is along the a-axis and b-axis (LP-a and LP-b excitation). The corresponding shear modes are shown in the inset of each panel. (d, e) Schematic illustration of the potential energy surface before (black line) and after (red line) the photoexcitation, and time evolution of Weyl points under two excitation conditions.

motion between the two layers is reversed and the noncentro-symmetric order is further enhanced.

The topological properties of WTe$_2$ are tunable via manipulating the polarization-dependent shear motion, as shown in Figures 11(d) and 11(e). Depending on the inter-layer shearing directions, all Weyl points (WPs) of opposite chirality will be annihilated or separated further to have extremely long Fermi arcs under LP-a and LP-b excitations, respectively. Meanwhile, the number of WPs can be freely modulated to zero, four, and eight, depending on the polarization and frequency of laser pulse.

The orbital-selective excitations in the vicinity of the Weyl node are the origin of switchable shear motion. Depending on atomic orbital features of Weyl bands and lin-ear light polarization, asymmetric excitation at the space-inversed k-points is achieved around the Weyl nodes with the photon energy lying in the range of $0.5 \sim 0.8$ eV. Accord-ing to the group theory analysis and dipole selection rule, we find that under LP-a excitation, $\langle d_{z^2}|S_x|p_x\rangle$ and $\langle d_{z^2}|S_x|d_{xz}\rangle$ are two dominant transition pathways along $W - \Gamma$, where W denotes the WP nearly on the high-symmetry line $\Gamma - X$, whereas under LP-b excitation, electronic transition along the W-X, i.e., $\langle d_{yz}|S_y|d_{z^2}\rangle$ is the most important pathway. Under the other excitation condition, these characteristic

transitions are forbidden due to the breaking of reflection symmetries. On the other hand, electrons will be excited to high-energy conductions bands by higher energy pho-tons, making the absorption process is marginal relevance to the Weyl physics and polarization isotropic. Based on above discussions, phase diagram relevant to the evolution of WP separation as a function of photon energy and inci-dent direction is constructed.

Notice that the orbital-selective excitation discussed here is different from the well-known spin selection rules, though both of them can uniquely determine the electronic transition pathways around the Weyl cone. In the latter case, the spin is flipped with absorption of a circularly polarized photon, leading to asymmetric excitations along the driving direction [76, 77]. The coupling between the chirality of the Weyl node and laser helicity is the dominant factor. Therefore, based on first-principles rt-TDDFT simulations, we provide a new insight into controlling Berry flux field singularity around the Weyl nodes.

3.2.4. Outlook.

In this review, we discussed a set of results that provide important insights into ultrafast engineering of crystal structures with light. Compared with the current established methods (e.g., strain, doping, static electric field,

and thermal annealing), photoexcitation offers several unique advantages in realizing phase transitions, including fast (femto- or picosecond) timescales, selectivity of desired structural distortions by precisely controlled laser parameters, and the potential to dynamically modulate the microscopic couplings. It enables a more detailed understanding of the relevant interactions among microscopic degrees of freedom as well as their dynamic behaviors in the time domain.

The creation and control of phases through light-matter couplings have been widely explored for the design of new functionalities. For example, the photoinduced structuring of 1T-TaS$_2$ emerges as a new avenue for memory devices in low-temperature circuitry [78], and the optical controlled phase transition in monolayer MoTe$_2$ has enabled an Ohmic heterophase homojunction necessary for improved transistor function [17]. To achieve the rational design of new functionalities, more attention should be paid to searching for new paradigms of material synthesis (e.g., fabricating van der Waals heterostructures) that enable the precise non-equilibrium control, and to theoretical frameworks that provide principles to achieve nonthermal phase transition pathways [79].

4. Conclusions

In summary, we present the TDAP, an ab initio method that is developed to provide an efficient tool to enable accurate simulations of light-induced nonequilibrium phenomena in complex systems. The use of NAO has provided flexibility and credibility to do large-scale simulations in low-dimensional materials and solids. The real-time evolution of coupled dynamics of photons, electrons, and phonon allows us to describe highly nonlinear processes from first-principle, without having to resort to the perturbation theory.

We have demonstrated its capability through illustrative examples, including the strategies to optimize solid-state high-harmonic performance via applying strain or two-color pulse, and its potential applications in reconstructing ground and excited state properties of target materials. Meanwhile, we also show that the explicit phase transition pathways can be revealed in CDW and topological materials, the emergence of hidden states, and the corresponding changes in electronic properties highlight the predictive power of the present approach. The HHG and structural phase transitions represent two important nonlinear responses to intense laser pulses in different timescales (i.e., sub-100 femtosecond versus several picoseconds), where the photon-electron and electron-phonon interactions are dominant, respectively.

Conventionally, the classical approximations of nuclear motions are good enough to obtain reliable results, as discussed in this paper. To further consider nuclear quantum effects, a practical computational scheme that goes beyond the Ehrenfest dynamics is highly desirable, where the rt-TDDFT and the ring polymer molecular dynamics (RPMD) can be combined to gain a full quantum description of electronic-nuclear states (i.e., the RP-TDAP approach) [80]. By comparing the theoretical and experimental results, our approaches have been demonstrated effective and efficient in treating a wide range of ultrafast quantum dynamical processes. We expect that they could be part of the standard tools for physicists, chemists, and materials scientists who are interested in ultrafast dynamics in broader fields.

Conflicts of Interest

The authors declare no competing interests.

Authors' Contributions

M.G. wrote the original draft, and all authors contributed to the analysis and discussion of the data and the writing of the manuscript. S.M. conceived the idea and supervised this project as a whole.

Acknowledgments

References

[1] F. Giustino, "Electron-phonon interactions from first principles," *Reviews of Modern Physics*, vol. 89, no. 1, article 015003, 2017.

[2] C.-Z. Chang, J. Zhang, X. Feng et al., "Experimental observation of the quantum anomalous Hall effect in a magnetic topological insulator," *Science*, vol. 340, no. 6129, pp. 167–170, 2013.

[3] N. P. Armitage, E. J. Mele, and A. Vishwanath, "Weyl and Dirac semimetals in three-dimensional solids," *Reviews of Modern Physics*, vol. 90, no. 1, article 015001, 2018.

[4] S. Y. Kruchinin, F. Krausz, and V. S. Yakovlev, "Colloquium: strong-field phenomena in periodic systems," *Reviews of Modern Physics*, vol. 90, no. 2, article 021002, 2018.

[5] M. F. Ciappina, J. A. Pérez-Hernández, A. S. Landsman et al., "Attosecond physics at the nanoscale," *Reports on Progress in Physics*, vol. 80, no. 5, article 054401, 2017.

[6] F. Krausz and M. Ivanov, "Attosecond physics," *Reviews of Modern Physics*, vol. 81, no. 1, pp. 163–234, 2009.

[7] P. Á. Corkum and F. Krausz, "Attosecond science," *Nature Physics*, vol. 3, no. 6, pp. 381–387, 2007.

[8] F. Rossi and T. Kuhn, "Theory of ultrafast phenomena in photoexcited semiconductors," *Reviews of Modern Physics*, vol. 74, p. 895, 2002.

[9] H. Yanagisawa, C. Hafner, P. Doná et al., "Optical control of field-emission sites by femtosecond laser pulses," *Physical Review Letters*, vol. 103, no. 25, 2009.

[10] S. Zherebtsov, T. Fennel, J. Plenge et al., "Controlled near-field enhanced electron acceleration from dielectric nanospheres with intense few-cycle laser fields," *Nature Physics*, vol. 7, no. 8, pp. 656–662, 2011.

[11] T. Brabec and F. Krausz, "Intense few-cycle laser fields: frontiers of nonlinear optics," *Reviews of Modern Physics*, vol. 72, no. 2, pp. 545–591, 2000.

[12] S. Ghimire and D. A. Reis, "High-harmonic generation from solids," *Nature Physics*, vol. 15, no. 1, pp. 10–16, 2019.

[13] N. Yoshikawa, T. Tamaya, and K. Tanaka, "High-harmonic generation in graphene enhanced by elliptically polarized light excitation," *Science*, vol. 356, no. 6339, pp. 736–738, 2017.

[14] D. Park and Y. Ahn, "Ultrashort field emission in metallic nanostructures and low-dimensional carbon materials," *Advances in Physics: X*, vol. 5, no. 1, article 1726207, 2020.

[15] S. Zhou, K. Chen, M. T. Cole et al., "Ultrafast field-emission electron sources based on nanomaterials," *Advanced Materials*, vol. 31, no. 45, article 1805845, 2019.

[16] A. Sood, X. Shen, Y. Shi et al., "Universal phase dynamics in VO2 switches revealed by ultrafast operando diffraction," *Science*, vol. 373, no. 6552, pp. 352–355, 2021.

[17] S. Cho, S. Kim, J. H. Kim et al., "Phase patterning for ohmic homojunction contact in MoTe2," *Science*, vol. 349, no. 6248, pp. 625–628, 2015.

[18] A. Yurtsever, R. M. van der Veen, and A. H. Zewail, "Subparticle ultrafast spectrum imaging in 4D electron microscopy," *Science*, vol. 335, no. 6064, pp. 59–64, 2012.

[19] M. Gulde, S. Schweda, G. Storeck et al., "Ultrafast low-energy electron diffraction in transmission resolves polymer/graphene superstructure dynamics," *Science*, vol. 345, no. 6193, pp. 200–204, 2014.

[20] D. M. Fritz, D. A. Reis, B. Adams et al., "Ultrafast bond softening in bismuth: mapping a solid's interatomic potential with X-rays," *Science*, vol. 315, no. 5812, pp. 633–636, 2007.

[21] E. Runge and E. K. U. Gross, "Density-functional theory for time-dependent systems," *Physical Review Letters*, vol. 52, no. 12, pp. 997–1000, 1984.

[22] M. Noda, S. A. Sato, Y. Hirokawa et al., "SALMON: Scalable Ab-initio Light-Matter simulator for Optics and Nanoscience," *Computer Physics Communications*, vol. 235, pp. 356–365, 2019.

[23] N. Tancogne-Dejean, M. J. T. Oliveira, X. Andrade et al., "Octopus, a computational framework for exploring light-driven phenomena and quantum dynamics in extended and finite systems," *The Journal of Chemical Physics*, vol. 152, no. 12, article 124119, 2020.

[24] C. A. Ullrich, *Time-Dependent Density-Functional Theory: Concepts and Applications (OUP)*, Oxford University Press (OUP), Oxford, 2011.

[25] C. Si, D. Choe, W. Xie et al., "Photoinduced vacancy ordering and phase transition in MoTe2," *Nano Letters*, vol. 19, no. 6, pp. 3612–3617, 2019.

[26] N. Tancogne-Dejean, M. A. Sentef, and A. Rubio, "Ultrafast modification of Hubbard U in a strongly correlated material: ab initio high-harmonic generation in NiO," *Physical Review Letters*, vol. 121, no. 9, article 097402, 2018.

[27] M. H. Beck, A. Jäckle, G. A. Worth, and H.-D. Meyer, "The multiconfiguration time-dependent Hartree (MCTDH) method: a highly efficient algorithm for propagating wave-packets," *Physics Reports*, vol. 324, no. 1, pp. 1–105, 2000.

[28] B. F. Curchod and T. J. Martínez, "Ab initio nonadiabatic quantum molecular dynamics," *Chemical Reviews*, vol. 118, no. 7, pp. 3305–3336, 2018.

[29] J. C. Tully and R. K. Preston, "Trajectory surface hopping approach to nonadiabatic molecular collisions: the reaction of H+ with D2," *The Journal of Chemical Physics*, vol. 55, no. 2, pp. 562–572, 1971.

[30] B. F. Curchod, I. Tavernelli, and U. Rothlisberger, "Trajectory-based solution of the nonadiabatic quantum dynamics equa-tions: an on-the-fly approach for molecular dynamics simula-tions," *Physical Chemistry Chemical Physics*, vol. 13, no. 8, pp. 3231–3236, 2011.

[31] D. Mac Kernan, G. Ciccotti, and R. Kapral, "Trotter-based simulation of quantum-classical dynamics," *The Journal of Physical Chemistry B*, vol. 112, no. 2, pp. 424–432, 2008.

[32] F. Agostini, S. K. Min, A. Abedi, and E. Gross, "Quantum-classical nonadiabatic dynamics: coupled-vs independent-trajectory methods," *Journal of Chemical Theory Computation*, vol. 12, no. 5, pp. 2127–2143, 2016.

[33] J. Tully, "Mixed quantum–classical dynamics," *Faraday Discussions*, vol. 110, pp. 407–419, 1998.

[34] H. D. Meyera and W. H. Miller, "A classical analog for electronic degrees of freedom in nonadiabatic collision processes," *The Journal of Chemical Physics*, vol. 70, no. 7, pp. 3214–3223, 1979.

[35] S. Meng and E. Kaxiras, "Real-time, local basis-set implementation of time-dependent density functional theory for excited state dynamics simulations," *The Journal of Chemical Physics*, vol. 129, no. 5, article 054110, 2008.

[36] C. Lian, M. Guan, S. Hu, J. Zhang, and S. Meng, "Photoexcitation in solids: first-principles quantum simulations by real-time TDDFT," *Advanced Theory and Simulations*, vol. 1, no. 8, article 1800055, 2018.

[37] P. You, D. Chen, C. Lian, C. Zhang, and S. Meng, "First-principles dynamics of photoexcited molecules and materials towards a quantum description," *Wiley Interdisciplinary Reviews: Computational Molecular Science*, vol. 11, no. 2, 2021.

[38] M. Guan, S. Hu, H. Zhao, C. Lian, and S. Meng, "Toward attosecond control of electron dynamics in two-dimensional materials," *Applied Physics Letters*, vol. 116, no. 4, article 043101, 2020.

[39] Y. Cheng, H. Hong, H. Zhao et al., "Ultrafast optical modulation of harmonic generation in two-dimensional materials," *Nano Letters*, vol. 20, no. 11, pp. 8053–8058, 2020.

[40] M.-X. Guan, C. Lian, S.-Q. Hu et al., "Cooperative evolution of intraband and interband excitations for high-harmonic generation in strained MoS$_2$," *Physical Review B*, vol. 99, no. 18, article 184306, 2019.

[41] H. Lakhotia, H. Y. Kim, M. Zhan, S. Hu, S. Meng, and E. Goulielmakis, "Laser picoscopy of valence electrons in solids," *Nature*, vol. 583, no. 7814, pp. 55–59, 2020.

[42] M. X. Guan, E. Wang, P. W. You, J. T. Sun, and S. Meng, "Manipulating Weyl quasiparticles by orbital-selective photo-excitation in WTe$_2$," *Nature Communications*, vol. 12, no. 1, p. 1885, 2021.

[43] C. Lian, S. J. Zhang, S. Q. Hu, M. X. Guan, and S. Meng, "Ultrafast charge ordering by self-amplified exciton-phonon dynamics in TiSe$_2$," *Nature Communications*, vol. 11, no. 1, p. 43, 2020.

[44] J. Zhang, C. Lian, M. Guan et al., "Photoexcitation induced quantum dynamics of charge density wave and emergence of a collective mode in 1T-TaS$_2$," *Nano Letters*, vol. 19, no. 9, pp. 6027–6034, 2019.

[45] K. Dewhurst, S. Sharma, L. Nordstrom et al., *The elk FP-LAPW code*, ELK, 2016, http://elk.sourceforge.net.

[46] A. O. Dohn, E. Ö. Jónsson, G. Levi et al., "Grid-based projector augmented wave (GPAW) implementation of quantum mechanics/molecular mechanics (QM/MM) electrostatic embedding and application to a solvated diplatinum complex," *Journal of Chemical Theory and Computation*, vol. 13, no. 12, pp. 6010–6022, 2017.

[47] S. K. Sundaram and E. Mazur, "Inducing and probing non-thermal transitions in semiconductors using femtosecond laser pulses," *Nature Materials*, vol. 1, no. 4, pp. 217–224, 2002.

[48] D. B. Williams and C. B. Carter, *Transmission Electron Microscopy*, Springer, 1996.

[49] W. Yuan, D. Zhang, Y. Ou et al., "Direct in situ TEM visualization and insight into the facet-dependent sintering behaviors of gold on TiO_2," *Angewandte Chemie*, vol. 130, no. 51, pp. 17069–17073, 2018.

[50] J. C. Johannsen, S. Ulstrup, F. Cilento et al., "Direct view of hot carrier dynamics in graphene," *Physical Review Letters*, vol. 111, no. 2, article 027403, 2013.

[51] P. Hein, S. Jauernik, H. Erk et al., "Mode-resolved reciprocal space mapping of electron-phonon interaction in the Weyl semimetal candidate *Td*-WTe_2," *Nature Communications*, vol. 11, no. 1, p. 2613, 2020.

[52] S. Ghimire, A. D. DiChiara, E. Sistrunk, P. Agostini, L. F. DiMauro, and D. A. Reis, "Observation of high-order harmonic generation in a bulk crystal," *Nature Physics*, vol. 7, no. 2, pp. 138–141, 2011.

[53] J. L. Krause, K. J. Schafer, and K. C. Kulander, "High-order harmonic generation from atoms and ions in the high intensity regime," *Physical Review Letters*, vol. 68, no. 24, pp. 3535–3538, 1992.

[54] F. Yao, C. Liu, C. Chen et al., "Measurement of complex optical susceptibility for individual carbon nanotubes by elliptically polarized light excitation," *Nature Communications*, vol. 9, no. 1, p. 3387, 2018.

[55] G. Vampa, T. Hammond, N. Thiré et al., "All-optical reconstruction of crystal band structure," *Physical Review Letters*, vol. 115, no. 19, article 193603, 2015.

[56] T. T. Luu and H. J. Wörner, "Measurement of the Berry curvature of solids using high-harmonic spectroscopy," *Nature Communications*, vol. 9, no. 1, p. 916, 2018.

[57] L. Li, P. Lan, X. Zhu et al., "Reciprocal-space-trajectory perspective on high-harmonic generation in solids," *Physical Review Letters*, vol. 122, no. 19, article 193901, 2019.

[58] D. Bauer and K. K. Hansen, "High-harmonic generation in solids with and without topological edge states," *Physical Review Letters*, vol. 120, no. 17, article 177401, 2018.

[59] S. Hüller and J. Meyer-ter-Vehn, "High-order harmonic radiation from solid layers irradiated by subpicosecond laser pulses," *Physical Review A*, vol. 48, no. 5, pp. 3906–3909, 1993.

[60] P. Kálmán and T. Brabec, "Generation of coherent hard-x-ray radiation in crystalline solids by high-intensity femtosecond laser pulses," *Physical Review A*, vol. 52, no. 1, pp. R21–R24, 1995.

[61] G. Vampa, C. McDonald, G. Orlando, D. Klug, P. Corkum, and T. Brabec, "Theoretical analysis of high-harmonic generation in solids," *Physical Review Letters*, vol. 113, no. 7, article 073901, 2014.

[62] D. Golde, T. Meier, and S. W. Koch, "High harmonics generated in semiconductor nanostructures by the coupled dynamics of optical inter- and intraband excitations," *Physical Review B*, vol. 77, no. 7, article 075330, 2008.

[63] Y. Kobayashi, C. Heide, H. K. Kelardeh et al., "Polarization flipping of even-order harmonics in monolayer transition-metal dichalcogenides," *Ultrafast Science*, vol. 2021, article 9820716, pp. 1–9, 2021.

[64] E. Goulielmakis, M. Schultze, M. Hofstetter et al., "Single-cycle nonlinear optics," *Science*, vol. 320, no. 5883, pp. 1614–1617, 2008.

[65] B. Xue, Y. Tamaru, Y. Fu et al., "A custom-tailored multi-TW optical electric field for gigawatt soft-X-ray isolated attosecond pulses," *Ultrafast Science*, vol. 2021, article 9828026, pp. 1–13, 2021.

[66] J. Mauritsson, J. M. Dahlström, E. Mansten, and T. Fordell, "Sub-cycle control of attosecond pulse generation using two-colour laser fields," *Journal of Physics B: Atomic, Molecular and Optical Physics*, vol. 42, no. 13, article 134003, 2009.

[67] I. J. Kim, C. M. Kim, H. T. Kim et al., "Highly efficient high-harmonic generation in an orthogonally polarized two-color laser field," *Physical Review Letters*, vol. 94, no. 24, article 243901, 2005.

[68] X. Zhu, Y. Cao, J. Zhang, E. W. Plummer, and J. Guo, "Classification of charge density waves based on their nature," *Proceedings of the National Academy of Sciences of the United States of America*, vol. 112, no. 8, pp. 2367–2371, 2015.

[69] M. Calandra and F. Mauri, "Charge-density wave and superconducting dome in TiSe2 from electron-phonon interaction," *Physical Review Letters*, vol. 106, no. 19, 2011.

[70] C. Chen, B. Singh, H. Lin, and V. M. Pereira, "Reproduction of the charge density wave phase diagram in1T−$TiSe_2$ Exposes its excitonic character," *Physical Review Letters*, vol. 121, no. 22, article 226602, 2018.

[71] T. Rohwer, S. Hellmann, M. Wiesenmayer et al., "Collapse of long-range charge order tracked by time-resolved photoemission at high momenta," *Nature*, vol. 471, no. 7339, pp. 490–493, 2011.

[72] L. Perfetti, P. A. Loukakos, M. Lisowski et al., "Time evolution of the electronic structure of 1T-TaS_2 through the insulator-metal transition," *Physical Review Letters*, vol. 97, no. 6, article 067402, 2006.

[73] M. Eichberger, H. Schäfer, M. Krumova et al., "Snapshots of cooperative atomic motions in the optical suppression of charge density waves," *Nature*, vol. 468, no. 7325, pp. 799–802, 2010.

[74] E. J. Sie, C. M. Nyby, C. D. Pemmaraju et al., "An ultrafast symmetry switch in a Weyl semimetal," *Nature*, vol. 565, no. 7737, pp. 61–66, 2019.

[75] M. Y. Zhang, Z. X. Wang, Y. N. Li et al., "Light-induced subpicosecond lattice symmetry switch in$MoTe_2$," *Physical Review X*, vol. 9, no. 2, article 021036, 2019.

[76] R. Yu, H. Weng, Z. Fang, H. Ding, and X. Dai, "Determining the chirality of Weyl fermions from circular dichroism spectra in time-dependent angle-resolved photoemission," *Physical Review B*, vol. 93, no. 20, article 205133, 2016.

[77] C.-K. Chan, N. H. Lindner, G. Refael, and P. A. Lee, "Photocurrents in Weyl semimetals," *Physical Review B*, vol. 95, no. 4, article 041104(R), 2017.

[78] R. V. Anže Mraz, M. Diego, A. Kranjec et al., "Energy efficient manipulation of topologically protected states in non-volatile ultrafast charge configuration memory devices," 2021, https://arxiv.org/abs/2103.04622.

[79] A. de la Torre, D. M. Kennes, M. Claassen, S. Gerber, J. W. McIver, and M. A. Sentef, "Nonthermal pathways to ultrafast control in quantum materials," 2021, https://arxiv.org/abs/2103.14888.

[80] P. You, J. Xu, C. Lian et al., "Quantum dynamics simulations: combining path integral nuclear dynamics and real-time TDDFT," *Electronic Structure*, vol. 1, no. 4, article 044005, 2019.